PCCP

Fundamental properties alkali-intercalated bilayer graphene nanoribbons

Journal:	*Physical Chemistry Chemical Physics*
Manuscript ID	CP-ART-05-2023-002266.R1
Article Type:	Paper
Date Submitted by the Author:	13-Jun-2023

Complete List of Authors:	Huynh, Thi My Duyen; National Cheng Kung University Department of Physics Hung, Guo-Song; National Cheng Kung University Department of Materials Science and Engineering Gumbs, Godfrey; Hunter College, CUNY, Physics and Astronomy Tran, Ngoc Thanh Thuy ; National Cheng Kung University, Hi-GEM Research Center

Fundamental properties of alkali-intercalated bilayer graphene nanoribbons

Thi My Duyen Huynh[1], Guo-Song Hung[2], Godfrey Gumbs[3,4], Ngoc Thanh Thuy Tran[5*]

[1]Department of Physics, National Cheng Kung University, Tainan 701, Taiwan

[2]Department of Materials Science and Engineering, National Cheng Kung University, Tainan 701, Taiwan

[3]Department of Physics and Astronomy, Hunter College of the City University of New York, New York 10065, United States.

[4]Donostia International Physics Center (DIPC), P de Manuel Lard Izabal, 4, 20018 San Sebastian, Basque Country, Spain.

[5]Hierachical Green-Energy Materials (Hi-GEM) Research Center, National Cheng Kung University, Tainan 701, Taiwan

*Email of the corresponding author: tranntt@phys.ncku.edu.tw

Abstract

Along with the inherent remarkable properties of graphene, adatom-intercalated graphene-related systems are expected to exhibit tunable electronic properties. The metal-based atoms could provide multi-orbital hybridizations with the out-of-plane π-bondings on the carbon honeycomb lattice, which dominates the fundamental properties of chemisorption systems. In this work, using the first-principles calculations, the feature-rich properties of alkali-metal intercalated graphene nanoribbons (GNRs) are investigated, including edge passivation, stacking configurations, intercalation sites, stability, charge density distribution, magnetic configuration, and electronic properties. There exists a transformation from finite gap semiconducting to metallic behaviors, indicating enhanced electrical conductivity. They arise from the cooperative or competitive relations among the significant chemical bonds, finite-size quantum confinement, edge structure, and stacking order. Moreover, the decoration of edge structures with hydrogen and oxygen atoms is considered to provide more information about the stability and

magnetization due to the ribbons' effect. These findings will be helpful for experimental fabrications and measurements for further investigation of GNRs-based materials.

Keywords: graphene nanoribbons (GNRs), first-principles, electronic properties, alkali intercalated GNRs, edge structure.

1. Introduction

Graphene nanoribbons (GNRs), a one-dimensional (1D) narrow strip of graphene, have motivated researchers to conduct numerous studies due to their fundamental properties such as easy synthesis and ability to open band gaps[1-4]. Through the 1D quantum confinement effects of GNR, the essential properties can be enhanced significantly, which could help overcome the limitations of 2D graphene with its zero-gap electronic structure[5]. Nanoribbon width and edge structure are crucial to the significant characteristics of GNRs, especially in bandgap engineering and magnetic configuration. The edges of GNRs can be characterized in two common types, namely armchair and zigzag (AGNRs and ZGNRs). The former belongs to non-magnetic (NM) semiconductors, whereas the latter are antiferromagnetic (AFM) ones[6]. In the cases of armchair ribbons, the ribbon width dependence has been reported with 3N rules that consider three types of ribbon configuration including 3N, 3N+1, and 3N+2, where N is the number of dimer lines. Consequently, the largest bandgap could be found in the 3N structure[7]. Generally, GNRs have been successfully synthesized under the top-down and bottom-up schemes including oxidation reaction[8, 9], chemical vapor deposition[10-12], and unzipping carbon nanotubes[13, 14]. However, roughness occurring at the ribbon edges during the synthesis process can reduce the mobility of GNRs because of the edge-scattering effects[15, 16]. To resolve this problem, adatom passivation at the edge is reported as an effective method[5, 16, 17]. The chemical bonds between adatoms and carbon atoms can reconstruct the edge structures and thereby drastically alter the electronic features. This study focuses on two typical adatom passivation types, H[5, 16, 17], and O[18-20], which are promising candidates in experimental and theoretical studies, respectively.

The properties of GNRs could be modulated by layered structures[21], chemical or physical modifications[22-26] such as doping[22, 27]/ adsorbing[28, 29], functionalizing[25, 26], or applying external fields[30, 31] for expanding the range of applications. It is worth mentioning that few-layer GNRs sharply contrast with monolayer systems in essential features, mainly owing to the various stacking configurations and

interlayer/intralayer spin distributions[32, 33]. The calculated results show that stacking configurations, especially AA and AB ones, reveal significant effects on electronic properties[33-35]. However, there are lacking studies regarding electronic properties, magnetic configurations, and geometric structures of O-passivated layered GNRs as compared to the H-GNRs one. Moreover, despite this H-GNRs are well studied theoretically, predictions are not consistent with one another related to the existence of magnetism and the planar/non-planar geometry[6, 36, 37]. Thus, more complete and accurate results are required to clearly identify the stacking-induced diverse behaviors in O- and H- passivated bilayer GNRs.

Along with structural alternation, chemical modification on GNRs is the most effective strategy used for creating dramatic changes between the semiconducting and metallic behaviors. For layered systems, adatom intercalated GNRs have attracted more interest and concerns[38-41] as promising for interconnect[42, 43] materials. Among intercalated atoms, alkali metals have received long-standing attention for intercalation[44-47] because of their simple electronic configuration and potential applications[43] in energy storage. The alkali-intercalated possibility has been demonstrated in bilayer graphene[11, 48] and MoS_2, indicating high charge transfer from the alkali atoms to the host material[49]. Besides, varying the concentration of alkali atoms intercalation could adjust the work function of graphene on Cu(111)[50] and the mean height of the carbon layer of graphene on Ir(111)[45] explained through charge transfer. Moreover, alkali intercalated graphene can be used to manipulate the electronic properties of graphene[46, 47] that could realize superconducting behavior[51] in bilayer graphene. Hence, alkali intercalated graphene systems suggest possible and potential ways for model study and applications that are expected to tune essential properties of bilayer GNRs. The single-orbitals of alkali atoms (Li/Na) are expected to enhance the conductivity that might have capable applications as interconnect materials or anode materials for Li/Na-ion batteries.

In this study, the fundamental properties of alkali-intercalated bilayer GNRs are systematically investigated by means of first-principles calculations. Both oxygen and hydrogen passivation are taken into account for comparison. The calculations focus on the formation energies, the adatom-carbon bond lengths, the optimal intercalated position, the adatom-dominated bands, the orbital projected density of states (PDOS), the charge density distributions, and the significant competitions of the carbon ribbon's edge and the adatoms passivation/intercalation in spin configurations. The essential properties arising from distinct types stacking layers, ribbon edge structures, as well as passivated and intercalated adatoms will be discussed in detail.

2. Computational Method

The first-principles calculations were performed with the use of the Vienna ab initio simulation software package (VASP)[52]. The projector augmented wave method was implemented to evaluate the electron-ion interactions, in which the electron-electron Coulomb interactions belong to the many-particle exchange and correlation energies under the Perdew-Burke-Ernzerhof (PBE)[53] generalized gradient approximation. The spin configurations are considered to explore the chemical absorption effects on the magnetic properties. A vacuum of 15 Å was set to suppress the van der Waals (vdW) interactions between neighboring slabs. Besides, a DFT-D3 vdW interaction was applied for examining interaction between two layers[54]. A plane-wave basis set with a maximum energy cut-off of 500 eV is available in the calculations of Bloch wave functions. For the criterion of energy and force, all atomic coordinates were relaxed until the force on each atom is less than 0.001 eV/Å and the energy convergence was set at 10^{-5} eV. The k-points of $15 \times 1 \times 1$ in Gamma symmetry and high-symmetric Γ-centered Brillouin zone grid were sampled for structural optimization and band energy calculations, respectively.

3. Results and discussion

3.1 Monolayer and bilayer GNRs

Edge passivation could control electronic properties of GNRs, which is used to precisely fabricate the ribbon structure. Among passivated atoms, hydrogen is reportedly the best theoretically; however, oxygen is highly considered in experiments[5, 16, 17, 19, 20, 36, 37, 55-58]. Due to the difference in chemical bonds and interaction with the edge, possible arrangements[59] of edge structures were considered both zigzag and armchair ribbons for both hydrogen and oxygen passivation. According to edge-formation energy per unit cell length, the distinct optimized zigzag and armchair H- and O-GNRs of monolayer is shown in Fig.S1 (Support information), indicated in different arrangements. Similarly, bilayer GNRs could also be constructed following these shapes (see Fig.1 and S2). In order to compare the stability of oxygen and hydrogen passivation, the formation energies calculation is also used, in which a smaller value indicates more favorable structures than others. The formation energy E_f of GNRs with hydrogen and oxygen edge passivation can be obtained as[59-61]

$$E_f = \left[E_{sys} - \left(n_C * E_C + \frac{n_{O/H}}{2} * Eo_{2/H_2}\right)\right]/2L \quad (1)$$

where E_{sys} is the total energy of GNR with oxygen or hydrogen termination; E_C and Eo_{2/H_2} are energy per atom of bulk AB graphite and oxygen or hydrogen molecules, respectively; n_C and $n_{O/H}$ are the numbers of carbon and oxygen or hydrogen atoms, respectively; and L is the length of the edge. According to the results for E_f for monolayer cases shown in Table 1, oxygen passivation exhibits more stable structures than that of H-cases based on smaller formation energies that is in good agreement with experimental studies[62-64]. However, hydrogen-passivated edges are theoretically reported to prevent the edge rearrangement due to passivating dangling bonds[5, 16, 17]. A hydrogen atom can cause further transformation of a sp^2 hybridized carbon atom at the edge to a sp^3 hybridized atom, resulting in hydrogen-saturated edges. Therefore, both kinds of passivation are considered for further constructing bilayer systems.

Following the arrangement of stacking in graphite[65-68], O- and H- passivated bilayer GNRs can be stacked in three types, namely AA, AB_α and AB_β, as shown in Fig.1 and Fig.S2, respectively. As described in these figures, AA is formed by arranging the section layer is directly on the top of the first layer while AB_α and AB_β are created by translating the second layer one C-C bond length along the armchair and zigzag direction, respectively. Table 1 illustrates the formation energies of oxygen and hydrogen passivation bilayer GNRs, where oxygen passivation dominates in terms of structural stability. The more stable phases of ZGNR and AGNR are, respectively, AA and AB_β for H-passivated cases and AB_α and AB_β for O-passivated cases. Therefore, these structures are further utilized for alkali intercalated systems. Additionally, the bandgap and interlayer distance are listed in this table, indicating the effect of stacking. For example, AA and AB_β exhibit metallic behavior while AB_α shows a very small gap structure in the H-ZGNR system. Also, AGNRs display larger-bandgap compared to ZGNRs both H- and O-passivated cases (see Table 1). Bilayer GNRs reveal various stackings leading to enlarge geometry and electronic properties of GNRs.

Table 1. Formation energies, bandgap, interlayer distance of H-/O-passivated monolayer and bilayer GNRs with AA, AB_α and AB_β stacked structures.

		Monolayer		Bilayer					
		H-passivated	O-passivated	H-passivated			O-passivated		
				AA	AB_α	AB_β	AA	AB_α	AB_β
ZGNRs									
E_f (eV)		-0.8075	-2.4722	-1.7149	-1.7048	-1.6916	-4.9482	-4.9815	-4.9768
E_g (eV)		0.4	0.175	M	0.035	M	0.013	M	0.11
d (Å)	d_1	--	--	3.017	3.383	3.688	4.081	3.38	3.56
	d_2	--	--	3.554	3.352	3.51	3.75	3.438	3.452
AGNRs									

E_f (eV)		-1.528	-2.8373	-2.6582	-2.7005	-2.7009	-5.6962	-5.7143	-5.7437
E_g (eV)		0.8	M	0.531	0.49	0.6	M	0.05	M
d (Å)	d_1	--	--	3.977	3.637	3.765	3.97	3.57	3.326
	d_2	--	--	3.95	3.692	3.404	3.683	3.462	3.52

M: metallic

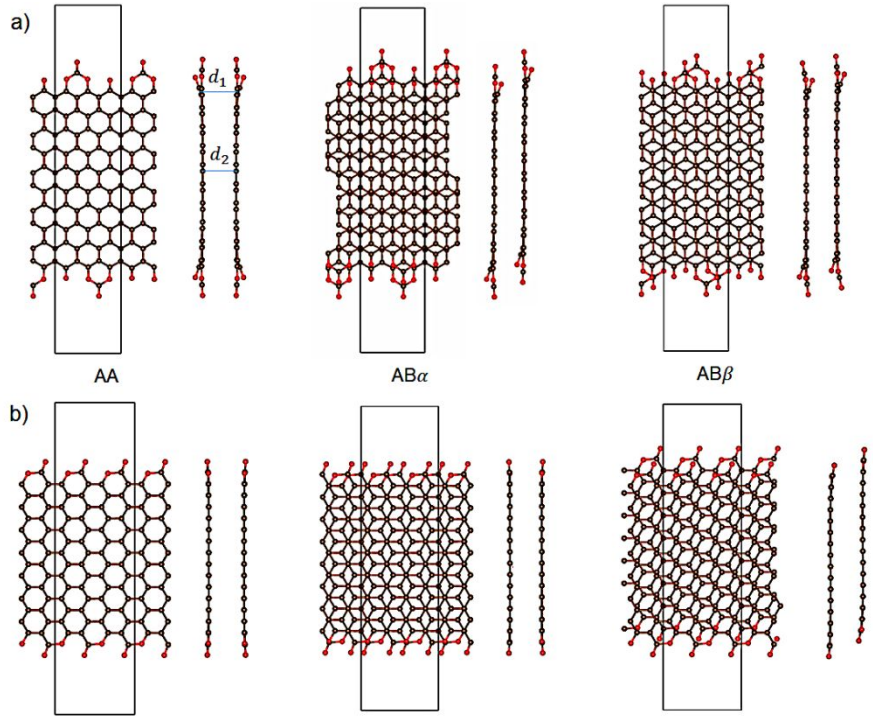

Fig. 1 The top and side views of bilayer O-passivated (a) ZGNRs and (b) AGNRs with considering three kinds of stacking AA, AB_α and AB_β, respectively. d_1 and d_2 describe interlayer distances of two layers near the edge and in the middle of the ribbon, respectively.

Electronic properties of GNRs are mainly determined by the edge structure, stackings, and quantum confinement effect. It is worth mentioning that bilayer GNRs are quite different from monolayer systems (see Fig.S3 in **Support Information**) in terms of energy dispersion, band overlap/bandgap, and van Hove singularities (vHs) in the DOS, as a result of stacking effect. Monolayer GNRs exhibit special 1D band structures owing to the honeycomb lattice symmetry, finite-

size quantum confinement, and edge structure. ZGNR (Fig.S3a) has a pair of partially flat valence and conduction bands nearest to the Fermi level (E_F) forming a direct gap of 0.4 eV, corresponding to wave functions localized at the zigzag boundaries due to the strong competition between quantum confinement and zigzag edge spin configuration (discussed later). For AGNRs, most of the energy dispersions are parabolic bands, while a few of them are partially flat ones. The low-lying electronic states within $\pm$ 2 eV and the deeper ones are, respectively, contributed by the π bonds of parallel $2p_z$ orbitals and the σ bonds of ($2s$,$2p_x$,$2p_y$) orbitals as described in the orbital-projected DOS.

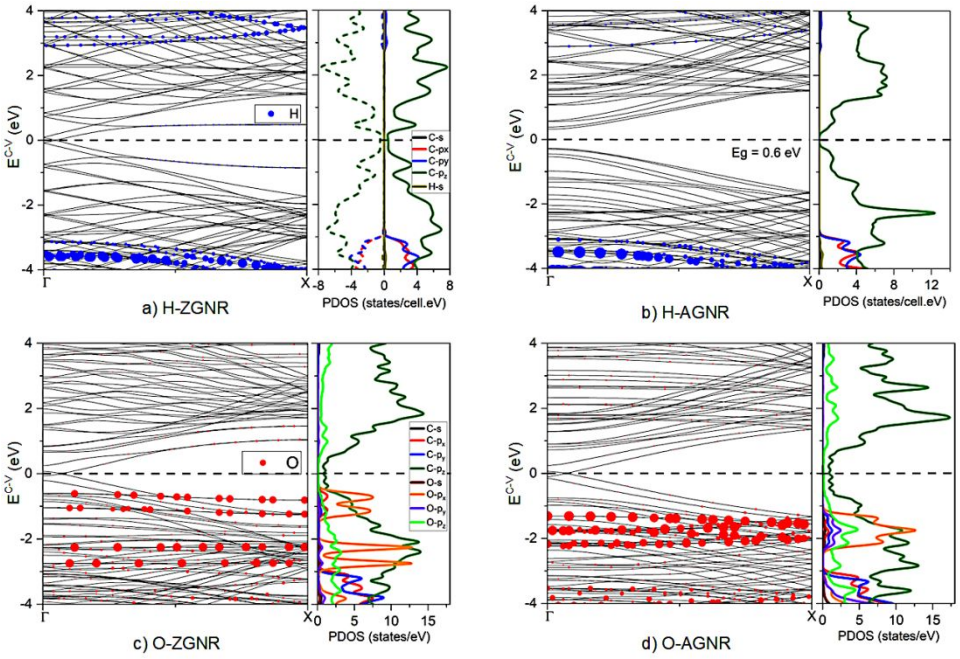

Fig. 2 Band energy structures and corresponding orbital-projected density of states (DOS) of H-passivated (a) ZGNR_AA, (b) AGNR_AB$_\beta$ and O-passivated (c) ZGNR_AB$_\alpha$, (d) AGNR_AB$_\beta$. Blue and red circles represent hydrogen and oxygen atom dominance, respectively. Solid and dash lines respectively describe spin up and down orbital density of states.

The electronic structures of H- and O-passivated bilayer GNRs (Fig.2) are systematically examined to determine the intercalation effect. The low-lying bands are composed of parabolic/linear and partially flat dispersions. Furthermore, the atomic edge illustrates distinct features in band structures, demonstrated in band gap and band overlap, in which H-AGNR (Fig.2b) belongs to direct

band gap of 0.6 eV, whereas a pair of linear bands intersecting at E_F is found in H-ZGNR (Fig.2a) and O-GNR (Fig.2c, d). Obviously, oxygen atoms perform a strong passivation effect, indicated in their significant dominance near the Fermi level while hydrogen atoms only weakly contribute at the middle-energy $|E^{c,v}| > 3$. There exist the sp^2s hybridizations in the C-H bonds, since there are peaks in the DOS dominated simultaneously by H-1s and C-(2s, $2p_x$, $2p_y$) orbital. On the other hand, the strong C-O bonds reveal the $2p_z$-$2p_z$ and (2s, $2p_x$, $2p_y$)- (2s, $2p_x$, $2p_y$) orbital hybridizations. The translation from π to co-exist π-σ bonds in the valence bands near the Fermi level between H- and O-case corresponding to the strong distribution of C-p_z and C-p_z, C-p_x,C-p_y, O-p_z orbitals in PDOS, respectively, further reveals the effect of atomic edge structure.

3.2 Alkali adatom-intercalated bilayer GNRs

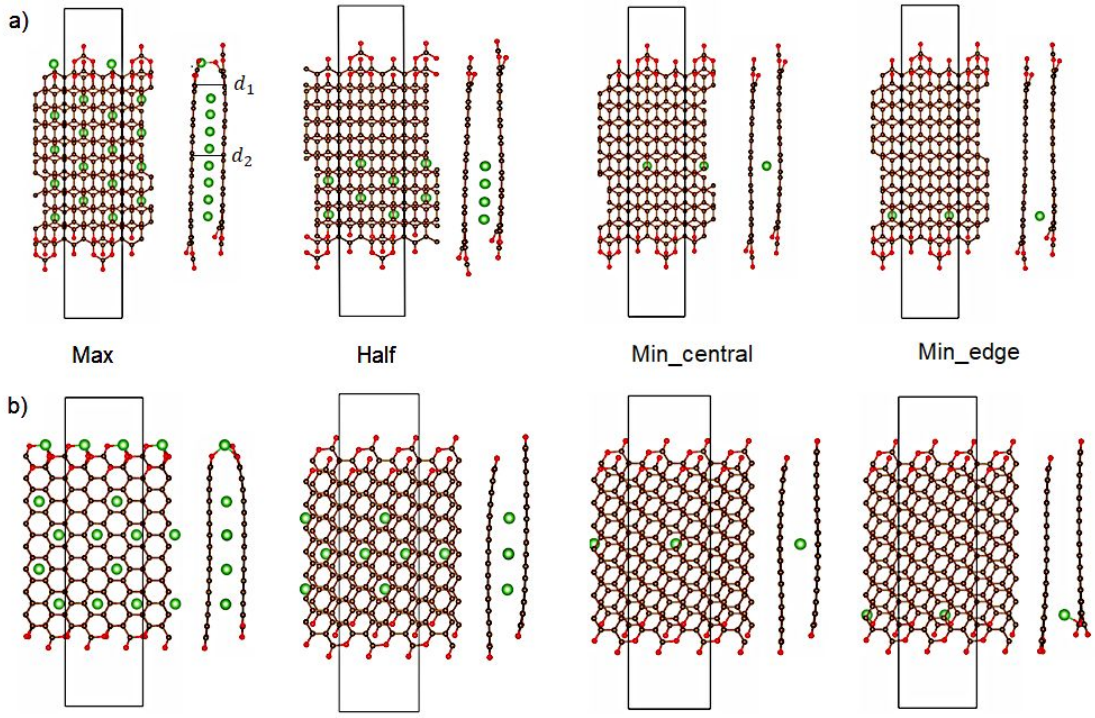

Fig. 3 Structural optimization of Alkali-intercalated GNRs in O-passivated (a) zigzag and (b) armchair edges with max, half, min_central, and min_edge intercalations. Green circles represent alkali atoms intercalated bilayer GNRs.

Alkali adatom intercalate bilayer GNRs can create an unusual geometric structure, being sensitive to the alkali (Li, Na) distribution and concentration. As discussed earlier, in the case of H- and O-passivated bilayer ZGNRs/AGNRs, the lower formation energies, prefer bilayer stacking corresponding to AA/AB_β and AB_α/AB_β, respectively. However, after Alkali intercalation, these stacking types are somehow shifted, indicating its effect on interlayer van der Waals interaction between layers, as shown in Fig.3. This is different from the case of Alkali intercalated graphite/layered graphene, in which the stable AB staking is shifted to AA stacking after intercalation. Based on the calculation result, the optimal position of alkali atoms is situated at the hollow site of one layer's honeycomb lattice. There are four main types of intercalations are investigated, namely fully-intercalation (max), half-intercalation (half), single-intercalation at the ribbon edge (min_edge), and single-intercalation at the center of ribbon (min_central), in which the max alkali distribution is similar to that of LiC_6 in graphite anodes[69]. In Fig.S4, the systems that are intercalated with H-GNRs are demonstrated using the same concentrations. The interlayer distance is specified in two values indicated by d_1 and d_2 at the edge and in the middle of the ribbon's width (Fig.3). The effects of adatom passivation and intercalation on layered GNRs are described in Table 2 and Fig.4. As shown in the table, interlayer distance is distinct depending on interaction between two stacking layers and the effect of intercalant as well as passivation. The distance could be increased by intercalated atoms, in which sodium cases show remarkably larger distance compared to lithium systems. In each intercalant system, the distance between position d_2 and d_1 is totally different based on intercalant position. Consider the central cases of ZGNRs as representative, d_2 is larger than d_1 because of intercalant located in the middle of the ribbon (see Table 2). Moreover, the intercalant could affect the C-C bond length in planar GNRs as shown in Fig.4 leading to the strongly non-uniform environment. Furthermore, intercalant exhibits a strong bonding with oxygen (A-O bonds) at the edge and modifies C-C and C-O bonds in this region. In contrast, A-H bonds are absent in all cases, indicating that oxygen is more active than

hydrogen that might come from the active 2p orbitals of oxygen atoms. Hence, alkali intercalated bilayer GNRs not only contribute to interaction between two layers but also adjust the chemical and structural environment of GNRs.

Table 2. Interlayer distance near the edge (d_1) and at the middle of the ribbon (d_2) of A-intercalated GNRs in both H- and O-passivated cases.

		H-passivated								O-passivated							
		Zigzag				Armchair				Zigzag				Armchair			
		(1)	(2)	(3)	(4)	(1)	(2)	(3)	(4)	(1)	(2)	(3)	(4)	(1)	(2)	(3)	(4)
Li	d_1	3.9	3.69	3.68	3.31	4.21	3.96	3.6	3.96	3.8	3.32	4.02	3.38	3.92	3.92	4.13	3.28
	d_2	3.72	3.65	3.66	3.76	4.2	3.84	3.43	3.89	4.02	4.04	3.52	3.93	3.8	4.0	3.52	3.92
Na	d_1	4.52	5.38	4.6	3.57	4.38	5.04	4.25	3.66	4.45	3.96	3.51	3.46	5.67	4.37	3.49	3.71
	d_2	4.45	4.24	3.62	4.79	4.63	4.33	3.65	4.13	6.83	5.38	3.52	4.7	6.84	5.27	3.53	4.78

(1): max, (2): half, (3): min_edge, (4): min_central

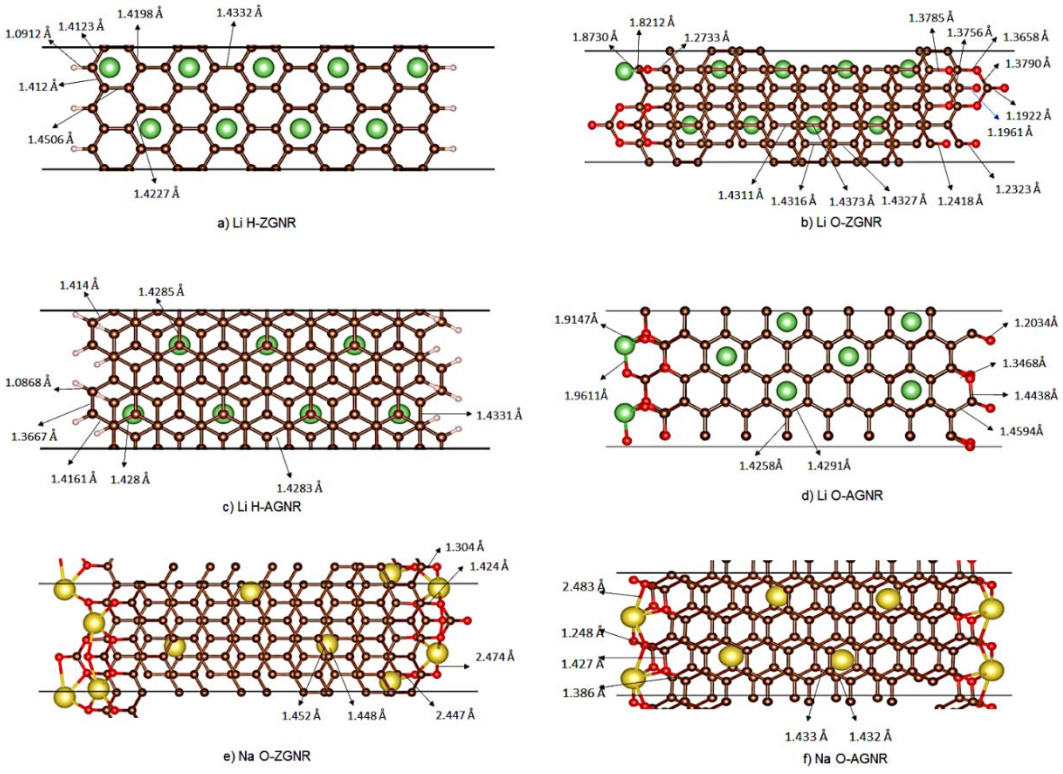

209 **Fig. 4** Chemical bond length (Å) of C-C, H-C, O-C and A-C bondings in the max case of Li-
210 intercalated (a) H-ZGNR, (b) O-ZGNR, (c) H-AGNR, (d) O-AGNR and Na-intercalated e) O-ZGNR, f)
211 O-AGNR indicates non-uniform environment after intercalating.

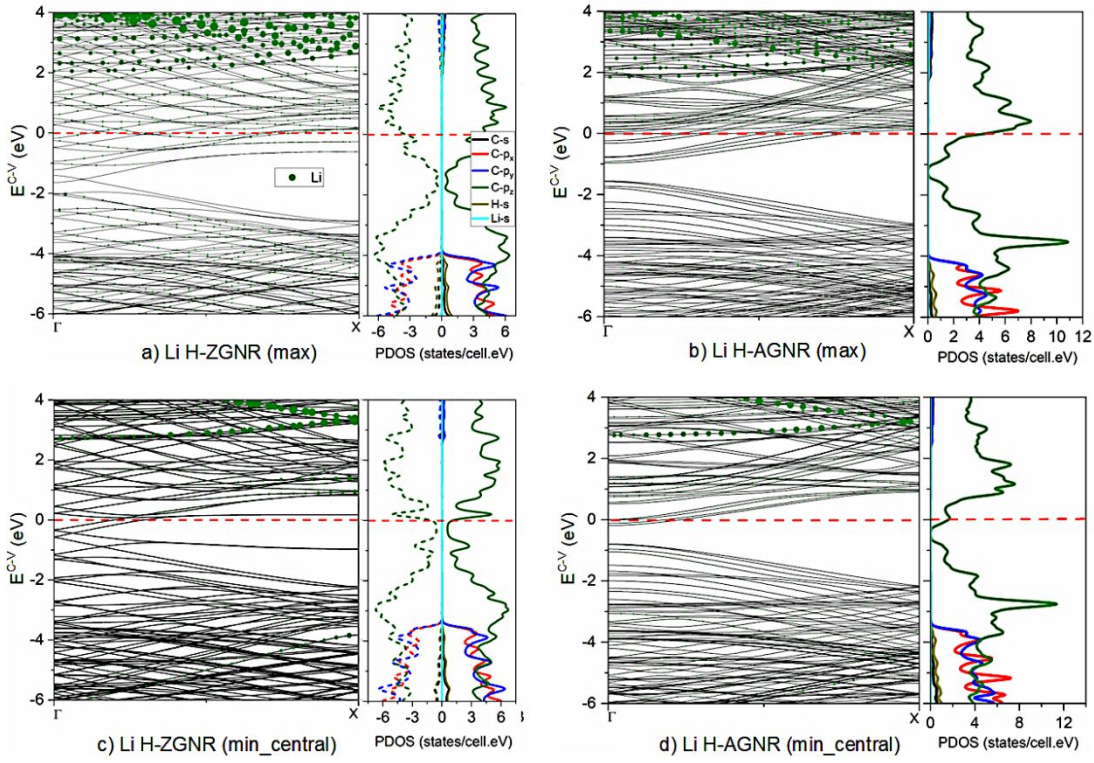

212

213 **Fig. 5** Band energy spectra of Li-intercalated bilayer (a) H-ZGNR, (b) H-AGNR in the max case and (c)
214 H-ZGNR, (d) H-AGNR in the min_central case. Green circles represent lithium atom dominance in
215 band structures. Solid and dash lines respectively describe spin up and down orbital density of states.

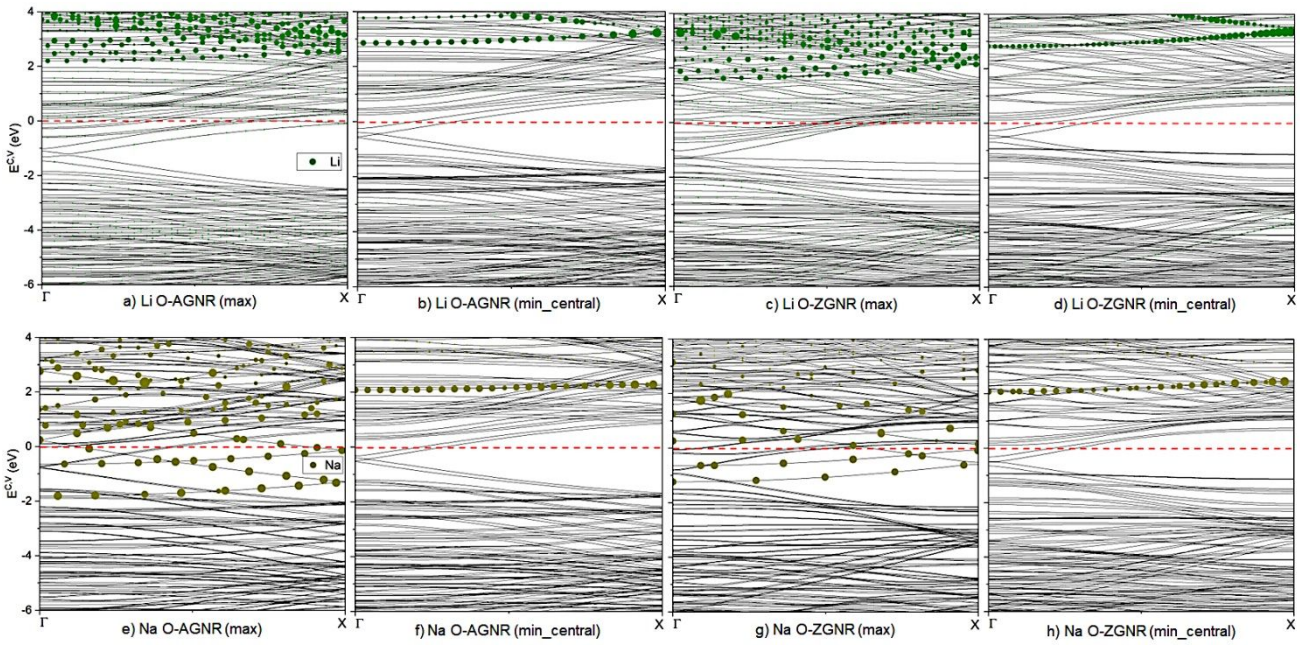

Fig. 6 Band energy structures of (a) Li- and (b) Na-intercalated O-GNRs in the max and min_central cases.

The alkali-intercalated GNRs exhibit feature-rich electronic properties, being dominated by the finite-size confinement, the critical orbital hybridizations in C-C, C-A, O/H-C and O-A bonds. Band energy spectra and orbital-projected DOS provide more information about these interactions through the contribution of orbitals and atoms in the system shown in Figs.5, 6 and 7. Accordingly, the band energy structure and corresponding orbital-projected DOS of Li-intercalated H-GNRs (Fig.5), band energy spectra of Li- and Na-intercalated O-GNRs (Fig.6), and orbital-projected DOS of Li-, Na-intercalated O-GNRs (Fig.7) are considered with the max and min_central cases. Other cases are also shown in Fig.S5 in **Support information** for displaying their characteristics. All A-intercalated GNRs exhibit metallic behavior due to the overlap between conduction and valence bands. Energy bands reveal significant blue shift with the shifting of E_F toward the conduction band about 0.5 eV to 1.5 eV, which is proportional to the Li concentration. Furthermore, there exists the edge-atom-induced valence and conduction bands in which lithium atoms reveal the strong effect in conduction bands based on adatom dominance. Apart from the contribution in conduction band, sodium atoms exhibit the

dominance in the valence band near the Fermi level (see Fig.6b), indicating the slightly distorted π bonding. To further verify the bandgap of these systems, the hybrid functional Heyd-Scuseria-Ernzerhof (HSE06)[70] was considered for a comparison. Band energy spectra of H-ZGNR and Li-intercalated H-ZGNR in the min_central case (Fig.S6) remain the metallic behavior as reported in PBE calculations with a good trend in vibration. Besides, the main characteristics of electronic structures are directly reflected in the DOS, as shown in Fig.7. Alkali intercalated GNRs reveal s-$2p_z$ and 2p-$2p_z$ orbital hybridizations in A-C/H-C and O-C belonging to hydrogen and oxygen passivation, respectively. Specifically, oxygen passivated cases indicate strong orbital hybridization due to 2p-$2p_z$ because of the outmost 2p orbitals of oxygen (see Fig.7) while this bond is absent in hydrogen cases. Moreover, A-intercalated HGNRs remain π bond near the Fermi level due to p_z orbitals with green curves (see Fig.5). On the other hand, σ and sp^3 bonds based on (p_x, p_y) and (s, p_x, p_y, p_z) orbitals make significant contributions to the valence DOS in oxygen passivated cases of both Li and Na intercalations (see Fig.7). Hydrogen and oxygen passivation display distinct features from each other in bilayer GNRs in both pristine and intercalated cases. Additionally, Na-intercalated systems show higher density of states compared to Li-intercalated cases because of more charge contribution which comes from its larger atom size. Hence, the intercalant not only affects structural characteristics such as bond length and interlayer distance, but also electronic features as mentioned in the energy bands and orbital-projected DOS.

In order to further comprehend the multi- or single-orbital hybridizations in A-C, H-C or O-C bonds, which dominate the essential properties, the spatial charge distributions have been taken into account. The charge density difference, created by subtracting the charge density of graphene and halogen atoms from that of the composite system, can provide very useful information about the chemical bondings and thus explain the dramatic changes of electronic structures. As crucial evidence for interaction, charge distribution of alkali intercalated GNRs provide more information about bonding

that exhibits the coexistence and common contribution of alkali and carbon atoms (see Fig.8 and Figs.S7, S8). In Fig.8, the charge density is exhibited in the side view for the max and min_central cases of A-intercalated O-GNRs. The charge distribution corresponding to intercalant and O-GNRs in cases of half and min_edge, and H-GNRs in cases of max and min_edge systems are also shown in Figs.S7 and S8. Obviously, the optimal intercalated GNRs display the buckled structure instead of the planar one as pristine monolayer case. This indicates that the σ- and π- bonds of carbon are somehow distorted due to the edge passivation and intercalation effect. According to the charge density, A-C and O-C bondings are revealed contribution in the region around lithium atoms indicating the van der Waals interactions and orbital hybridization in the system. Furthermore, there exist charge variations between alkali and carbon atoms, arising from the s-$2p_z$ orbital hybridization in A-C bonds and 2p-$2p_z$ orbital hybridization in O-C bonds. It is worth noting that the well-extended σ-bonding in graphene is hardly affected by alkali intercalation but dramatically affected by oxygen passivation, leading to the modifications on the carbon dominated valence bands. The π-bonds are distorted only near the adatom sites, and they behave like the normal extended states at other positions.

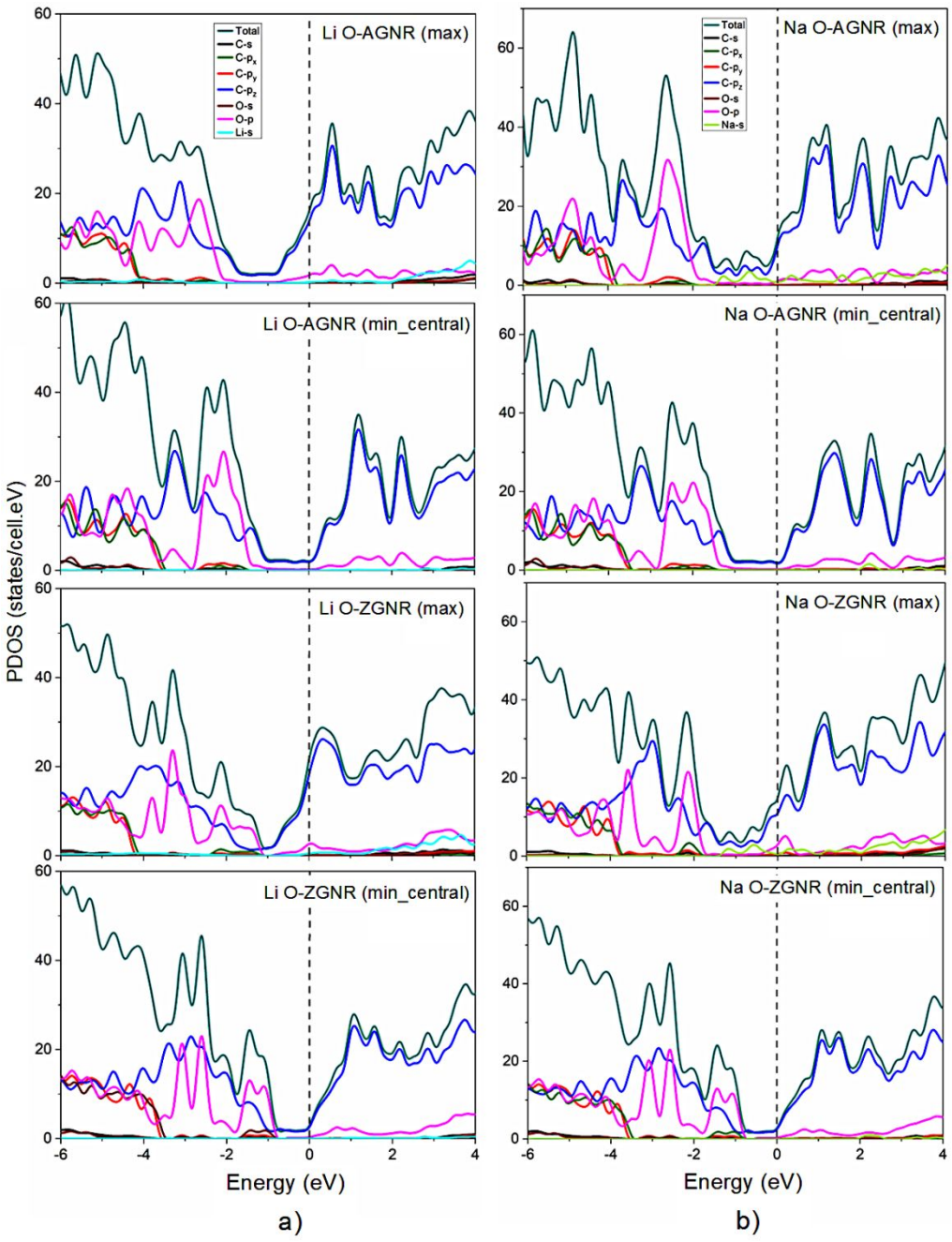

Fig. 7 Orbital-projected DOS of (a) Li- and (b) Na-intercalated O-GNRs in the max and min_central cases.

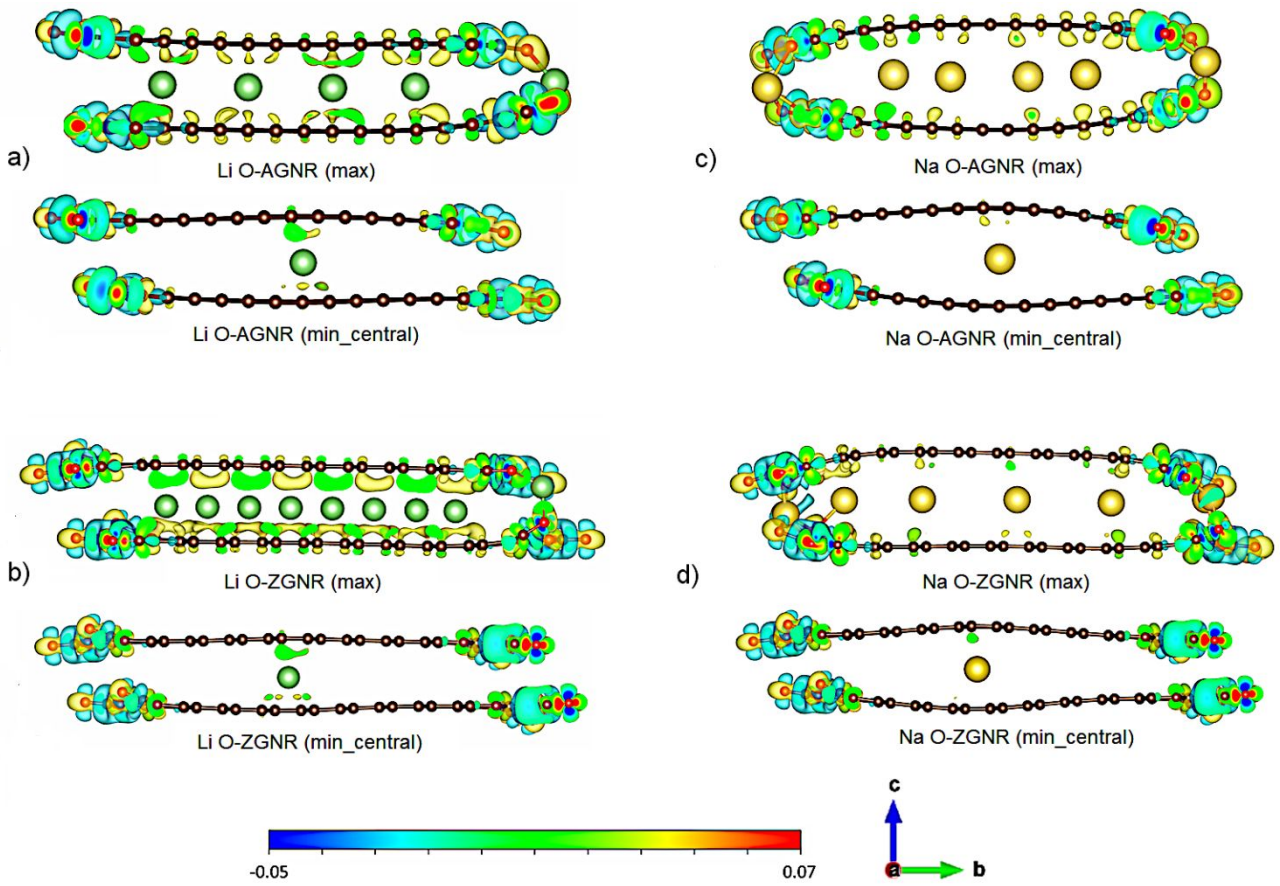

Fig. 8 The charge density difference of Li-intercalated (a) O-AGNRs, (b) O-ZGNRs, c) Na-intercalated (c) O-AGNRs, (d) O-ZGNRs in the max and min_central cases.

Interestingly, there are significant differences in magnetic configurations between O- and H-passivated GNRs which were not reported elsewhere previously. In cases of non-passivation GNR, it is well-known that the ZGNR belongs to AFM, while the armchair one is NM. This AFM has zero net magnetic moment, since two edges in a zigzag system are symmetric about the center of the nanoribbon (see Fig. S9). Based on our spin-polarized calculations, O-passivation cases display NM configurations for all the monolayer and bilayer structures, even with the zigzag edge. As shown previously in the electronic structures (Fig. 5, Fig 6, Fig. 7) and charge density (Fig. 8), the strong bonding between O atoms and ribbon edge's C atoms has destroyed the AFM configuration of non-passivated ZGNR. In cases of H-passivation, due to the weak s-$2p_z$ orbital hybridization in H-C bonds, the magnetic configuration remains the same as non-passivation case. For bilayer GNRs, the typical

spin configurations can be classified as AFM-AFM, FM-AFM, and FM-FM, corresponding to their intralayer-interlayer (single layer-bilayer) spin arrangements. The AFM-AFM and FM-AFM models as shown in Figs.9 (a-f) are the stable magnetic configurations for all three types of stacking AA, AB_{α} and AB_{β}, owing to the lower ground state energies (see Table S1). The magnetic moment on the edge atom (carbon edge) and total magnetic moment in single and bilayer are also listed in Table S2 of the Supporting Information. With AFM-AFM model (Figs. 9b, 9d, 9f), spin up and down are split into two edges within each layer (AFM intralayer spin arrangement). Looking at the bilayer as a whole, the interlayer spin arrangements are inverse on the same edge (AFM interlayer spin arrangement). Whereas FM-AFM cases (Figs. 9a, 9c, 9e, 9g), one layer presents spin-up while the other indicates spin-down configurations (FM intralayer spin arrangement). On the same edge of the bilayer, spin up and down are inverse (AFM interlayer spin arrangement). For FM-FM cases (Figs. 9h, 9i), each layer and the overall bilayer present spin-up dominated configurations. These aforementioned differences in edge passivation and spin configurations could lead to diverse electronic properties. Under intercalation (Fig.9 (g-i)), the spin configuration is strongly distorted. Intercalation at high concentrations can destroy the surrounding spin configuration due to strong bonds between intercalated atoms and carbons as illustrated in Fig. 9g for the half_edge case. In contrast, the spin distribution remains at the intercalation edge but is absent at the non-intercalation edge at low intercalation (Fig. 9h). Similar behavior could be observed in the case of Na adatoms (Fig. 9i). As shown by the significant difference in layer distance between the two edges of the ribbon, this could be the result of the vdW interaction effect on spin polarization. This effect of vdW on magnetic configuration is also observed in other layered systems[71].

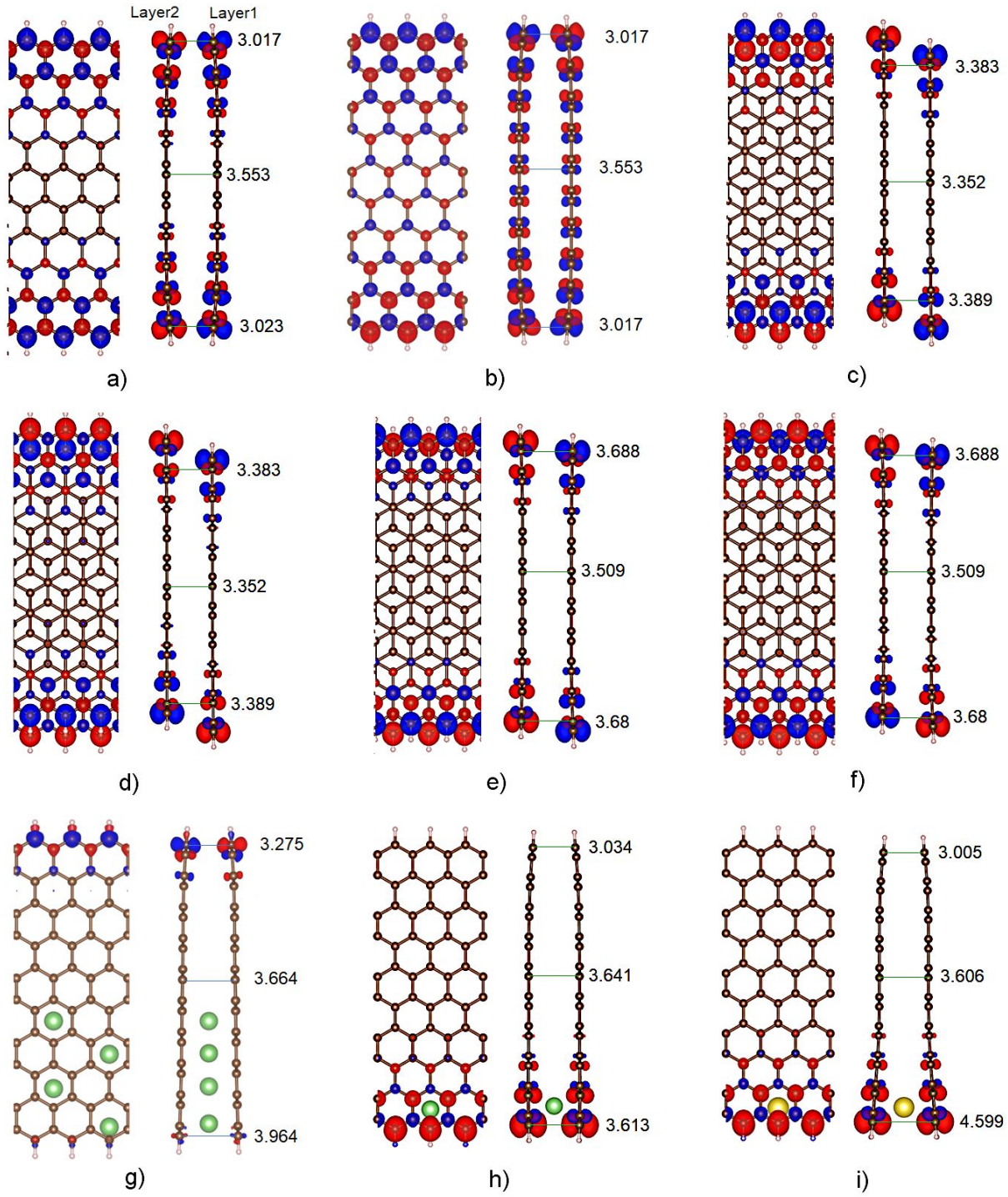

Fig. 9 The top and side views of spin distribution considering various magnetic configurations including (a) FM-AFM, (b) AFM-AFM in AA-stacked, (c) FM-AFM, (d) AFM-AFM in AB_{α}-stacked, (e) FM-AFM, (f) AFM-AFM in AB_{β}-stacked H-ZGNR. The spin displacement after intercalation of Li intercalated AA H-ZGNR in g) half, (h) min_edge cases, and (i) Na intercalated AA H-ZGNR in

min_edge case. Red and blue circles describe spin up and spin down distribution. The interlayer distances at two edges and center of the ribbon were also displayed.

Additionally, the main features of band structures and DOS could be examined by angle-resolved photoemission spectroscopy (ARPES) and scanning tunneling spectroscopy (STS) measurements. ARPES is an effective tool in identifying the diverse band structures of graphene-based systems, e.g., the 1D parabolic valence bands near the Γ point accompanied with band gaps and distinct energy spacings of AGNRs in the presence/absence of edge passivation[72, 73]. The greatly modified band structures of the Ti-absorbed graphene[74] or the red shift of 1.0-1.5 eV in the pi bands (n-type doping)[75] has been confirmed by using high-resolution ARPES. On the other hand, STS measurements of the dI/dV spectra, which is proportional to the local DOS, has confirmed the asymmetric peaks of 1D parabolic bands of GNRs[76, 77] and the opening of confinement energy gap[72, 78].

Regarding applications, intercalated systems are expected to play a role in the next and modern generation of materials which are technology nodes[4, 57, 69] including anodes, cathodes, electrolytes, and interconnects. Among them, interconnect performance of GNRs has become an emergent and fascinating structure in integrated circuits because of their limitations of speed. As shown in Figs.5, 6, and 7, the upward shift in the Fermi level of Li-intercalated GNRs energy bands corresponding to an increase in conductivity results from injection of carrier from the intercalate layer. Meanwhile, the increased interlayer distance after intercalation (see Table 2 and Fig.9) leads to higher mean free path (MFP) that supports the interconnect feature. The distributed perpendicular resistance between GNR layers depends on c-axis resistivity and interlayer spacing, in which the highly c-axis conductivity induces the enhanced interconnect with the effective resistance decreases. Instead of using Cu in interconnects, Li intercalation exhibits an improvement in the in-plane conductivity along the c axis of GNRs[43] which has been reported in experimental measurement about the function of interconnect such as lowest delay and energy delay product (EDP). Thus, Li/Na-intercalated GNRs have promise as a

potential candidate for interconnect applications[42, 43], suggesting that alkali intercalated systems could support this point. Besides, one of the most appealing properties of 2D materials is superconductivity which has been applied in recent material science. However, a superconducting state in pristine monolayer graphene has not been reported, leading to a manipulation in atomic structure to induce this feature in graphene or graphene-based systems. A DFT study on alkaline-intercalated bilayer graphene C_6XC_6 (X = K, Rb)[51] reveal metallic behavior, and a phonon-mediated superconducting state based on electron-phonon coupling was predicted with T_c ranging from 5.47-14.56K. At a Tc of 7.9-9.8K, superconductivity with strong electron-phonon coupling is also predicted in CaC_2 carbon ribbon structure[79]. Similar anticipations have been made for various graphite-intercalated compounds[79-82]. It is believed that phonons mediate the superconductivity in metal-intercalated carbon superconductors, with electron-phonon coupling as the underlaying mechanism superconductivity[81-83]. Hence, Li/Na-intercalated GNRs with similar structures and metallic behavior may exhibit a phonon-mediated state. Generally, this work is hopeful that our findings can stimulate further experimental studies on essential and state-of-the-art properties of intercalated bilayer GNRs by verifying the results and predictions herein.

Concluding Remarks

In this work, layered GNR structures with hydrogen and oxygen passivation edges have been optimized by means of first-principles calculations. A comparison between two passivations was also considered in order to verify significant and distinct features, in which H-passivated cases exhibited magnetic configuration while the NM behavior was found in all O-passivated systems. AFM-AFM and FM-AFM configurations display stable magnetic structures in bilayer and intercalated H-GNRs, in which the significant effect of intercalation and vdW interaction was observed. Moreover, the alkali-metals-intercalated layered GNRs can induce metallic behaviors, indicating higher carrier density compared to the semiconducting pristine GNR ones. Furthermore, our systems suggest the application

in interconnect materials, or further research in superconducting states due to their metallic behavior. In each intercalated case, intercalant displays different features, resulted in interlayer distance, atom dominance in band energy and orbital distribution in DOS, in which sodium shows the stronger distribution in band energy and enlarged interlayer distance, as well as higher density of states. There are feature-rich geometric and electronic properties, being dominated by the finite-size confinement, edge passivation, Van der Waal interactions, and the critical orbital hybridizations in C-C, C-A, O-C, H-C and O-A bonds. The predicted geometric structures, electronic properties, and magnetic configurations are worthy of further experimental examinations. Hence, the present work should serve as a first step toward further investigation into other necessary properties of alkali-metals-intercalated GNRs for fabrication and potential devices.

Author contributions

Thi My Duyen Huynh: conceptualization, model building, methodology, software, validation, original draft preparation, writing-reviewing and editing.

Guo-Song Hung: model building, data curation, methodology, software.

Godfrey Gumbs: validation, reviewing and editing.

Ngoc Thanh Thuy Tran: conceptualization, model building, data curation, visualization, methodology, validation, reviewing and editing, supervision.

Conflicts of interest

There are no conflicts to declare.

Acknowledgments

This work was supported by the Hierarchical Green-Energy Materials (Hi-GEM) Research Center, National Cheng Kung University, and the Taiwan National Science and Technology Council (NSTC)

under the project numbers 108-2112-M-006-022-MY3 and 111-2221-E-006-097-MY3. G.G. would like to acknowledge the support from the Air Force Research Laboratory (AFRL) through Grant No. FA9453-21-1-0046.

References

1. Deepika, T. J. D. Kumar, A. Shukla and R. Kumar, *Phys. Rev. B*, 2015, **91**, 115428.
2. M. Y. Han, B. Ozyilmaz, Y. B. Zhang and P. Kim, *Phys. Rev. Lett.*, 2007, **98**, 206805.
3. M. Zhang, G. S. Li and L. P. Li, *J. Mater. Chem. C*, 2014, **2**, 1482-1488.
4. T. T. Zhang, S. Wu, R. Yang and G. Y. Zhang, *Front. Phys.*, 2017, **12**, 127206.
5. Y. H. Lu, R. Q. Wu, L. Shen, M. Yang, Z. D. Sha, Y. Q. Cai, P. M. He and Y. P. Feng, *Appl. Phys. Lett.*, 2009, **94**, 122111.
6. F. J. Owens, *J. Chem. Phys.*, 2008, **128**, 194701.
7. S.-Y. Lin, Thanh Thuy Tran, N., Chang, S.-L., Su, W.-P., & Lin, M.-F., *CRC Press*, 2018. ISSN: 9780367002299.
8. G. Ghigo, A. Maranzana and G. Tonachini, *Int. J. Quantum Chem.*, 2016, **116**, 1281-1284.
9. S. Fujii and T. Enoki, *J. Am. Chem. Soc.*, 2010, **132**, 10034-10041.
10. E. K. Pefkianakis, G. Sakellariou and G. C. Vougioukalakis, *Arkivoc*, 2015, 167-192.
11. I. Mitchell, S. Irle and A. J. Page, *Phys. Chem. Chem. Phys.*, 2018, **20**, 19987-19994.
12. M. Sprinkle, M. Ruan, Y. Hu, J. Hankinson, M. Rubio-Roy, B. Zhang, X. Wu, C. Berger and W. A. de Heer, *Nat. Nanotechnol.*, 2010, **5**, 727-731.
13. W. Lu, G. D. Ruan, B. Genorio, Y. Zhu, B. Novosel, Z. W. Peng and J. M. Tour, *Acs Nano*, 2013, **7**, 2669-2675.
14. L. Y. Jiao, L. M. Xie and H. J. Dai, *Nano Res.*, 2012, **5**, 292-296.
15. D. Basu, M. J. Gilbert, L. F. Register, S. K. Banerjee and A. H. MacDonald, *Appl. Phys. Lett.*, 2008, **92**, 042114.
16. G. Wang, *Chem. Phys. Lett.*, 2012, **533**, 74-77.
17. Y. J. Liu, Z. Chen, L. J. Tong, J. Zhang and D. Q. Sun, *Comput. Mater. Sci.*, 2016, **117**, 279-285.
18. M. Y. Notash, A. R. Ebrahimzadeh, J. J. Sardroodi and B. Ghavami, *Applied Physics a-Materials Science & Processing*, 2018, **124**.
19. H. Y. Ge and G. Wang, *Chinese J. Struc. Chem.*, 2015, **34**, 641-649.
20. Y. C. Zeng, W. Tian and Z. H. Zhang, *Acta Phys. Sin.*, 2013, **62**, 236102.
21. J. W. Rhim and K. Moon, *Phys. Rev. B*, 2011, **84**, 035402.
22. H. Terrones, R. T. Lv, M. Terrones and M. S. Dresselhaus, *Rep. Prog. Phys.*, 2012, **75**, 062501.
23. K. Sheng, H. K. Yuan, H. Chen and Z. Y. Wang, *J. Phys. Chem. Solids*, 2020, **146**, 109623.
24. L. Daukiya, M. N. Nair, M. Cranney, F. Vonau, S. Hajjar-Garreau, D. Aubel and L. Simon, *Prog. Surf. Sci.*, 2019, **94**, 1-20.
25. Q. Tang, Z. Zhou and Z. F. Chen, *Nanoscale*, 2013, **5**, 4541-4583.
26. M. Di Giovannantonio, O. Deniz, J. I. Urgel, R. Widmer, T. Dienel, S. Stolz, C. Sanchez-Sanchez, M. Muntwiler, T. Dumslaff, R. Berger, A. Narita, X. L. Feng, K. Mullen, P. Ruffieux and R. Fasel, *Acs Nano*, 2018, **12**, 74-81.
27. S. Kawai, S. Saito, S. Osumi, S. Yamaguchi, A. S. Foster, P. Spijker and E. Meyer, *Nat. Commun.*, 2015, **6**., 8098.
28. N. Jung, A. C. Crowther, N. Kim, P. Kim and L. Brus, *Acs Nano*, 2010, **4**, 7005-7013.
29. H. S. Moon, J. H. Lee, S. Kwon, I. T. Kim and S. G. Lee, *Carbon Lett.*, 2015, **16**, 116-120.
30. N. Konobeeva and M. Belonenko, *Mod. Phys. Lett. B*, 2017, **31**, 36, 1750340.
31. H. X. Da, Z. Y. Li and L. Z. Sun, *J. Comput. Theor. Nanosci.*, 2013, **10**, 515-520.
32. A. M. Ilyin, V. V. Kudryashov and N. R. Guseinov, *J. Electrochem. Soc.*, 2015, **162**, A1544-A1546.
33. K. K. Paulla and A. A. Farajian, *J. Phys. Condens. Matter*, 2013, **25**, 115303.
34. Y. Mohammadi and B. A. Nai, *Solid State Commun.*, 2015, **201**, 76-81.

35. X. L. Zhong, R. Pandey and S. P. Karna, *Carbon*, 2012, **50**, 784-790.
36. S. Haffad, L. Benchallal, L. Lamiri, F. Boubenider, H. Zitoune, B. Kahouadji and M. Samah, *Acta Phys. Pol. A*, 2018, **133**, 1307-1313.
37. A. Garcia-Fuente, L. J. Gallego and A. Vega, *Phys. Chem. Chem. Phys.*, 2016, **18**, 22606-22616.
38. B. Xu, Y. H. Lu, Z. D. Sha, Y. P. Feng and J. Y. Lin, *Epl*, 2011, **94**, 27007.
39. O. Deniz, C. Sanchez-Sanchez, R. Jaafar, N. Kharche, L. Liang, V. Meunier, X. Feng, K. Mullen, R. Fasel and P. Ruffieux, *Chem. Commun.*, 2018, **54**, 1619-1622.
40. Y. Xie, W. T. Zhang, S. Cao, A. N. Zhou and J. M. Zhang, *Physica E Low Dimens. Syst. Nanostruct.*, 2019, **106**, 114-120.
41. O. Deniz, C. Sanchez-Sanchez, T. Dumslaff, X. L. Feng, A. Narita, K. Mullen, N. Kharche, V. Meunier, R. Fasel and P. Ruffieux, *Nano Lett.*, 2017, **17**, 2197-2203.
42. J. K. Jiang, J. H. Kang, W. Cao, X. J. Xie, H. J. Zhang, J. H. Chu, W. Liu and K. Banerjee, *Nano Lett.*, 2017, **17**, 1482-1488.
43. A. K. Nishad and R. Sharma, *Ieee J. Electron Devices Soc.*, 2016, **4**, 485-489.
44. L. Speyer, S. Fontana, S. Cahen and C. Herold, *Microporous and Mesoporous Mater.*, 2020, **306**, 110344.
45. C. C. Silva, J. Q. Cai, W. Jolie, D. Dombrowski, F. H. F. zum Hagen, A. J. Martinez-Galera, C. Schlueter, T. L. Lee and C. Busse, *J. Phys. Chem. C*, 2019, **123**, 13712-13719.
46. H. C. Shin, S. J. Ahn, H. W. Kim, Y. Moon, K. B. Rai, S. H. Woo and J. R. Ahn, *Appl. Phys. Lett.*, 2016, **109**, 081603.
47. S. Ahmad, P. Miro, M. Audiffred and T. Heine, *Solid State Commun.*, 2018, **272**, 22-27.
48. T. Kaneko and R. Saito, *Surf. Sci.*, 2017, **665**, 1-9.
49. I. V. Chepkasov, M. Ghorbani-Asl, Z. I. Popov, J. H. Smet and A. V. Krasheninnikov, *Nano Energy*, 2020, **75,** 104927.
50. B. Cook, A. Russakoff and K. Varga, *Appl. Phys. Lett.*, 2015, **106**, 211601.
51. A. P. Durajski, K. M. Skoczylas and R. Szczesniak, *Phys. Chem. Chem. Phys.*, 2019, **21**, 5925-5931.
52. J. Hafner, *J. Comput. Chem.*, 2008, **29**, 2044-2078.
53. M. Ernzerhof and G. E. Scuseria, *J. Chem. Phys.*, 1999, **110**, 5029-5036.
54. S. Grimme, J. Antony, S. Ehrlich and H. Krieg, *J. Chem. Phys.*, 2010, **132**, 154104.
55. Y. B. Chu, T. Ragab, P. Gautreau and C. Basaran, *J. Nanomech. Micromech.*, 2015, **5**.
56. S. D. Wang, L. Y. Zhu, Q. A. Chen, J. L. Wang and F. Ding, *J. Appl. Phys.*, 2011, **109**, 053516.
57. X. Tong, Q. L. Wei, X. X. Zhan, G. X. Zhang and S. H. Sun, *Catalysts*, 2017, **7**.
58. C. X. Zhang, C. Y. He, L. Xue, K. W. Zhang, L. Z. Sun and J. X. Zhong, *Org. Electron.*, 2012, **13**, 2494-2501.
59. A. P. Seitsonen, A. M. Saitta, T. Wassmann, M. Lazzeri and F. Mauri, *Phys. Rev. B*, 2010, **82**, 115425.
60. M. Vanin, J. Gath, K. S. Thygesen and K. W. Jacobsen, *Phys. Rev. B*, 2010, **82**, 195411.
61. M. M. Monshi, S. M. Aghaei and I. Calizo, *Rsc Advances*, 2017, **7**, 18900-18908.
62. Z. S. Geng, B. Hahnlein, R. Granzner, M. Auge, A. A. Lebedev, V. Y. Davydov, M. Kittler, J. Pezoldt and F. Schwierz, *Annalen Der Physik*, 2017, **529**.
63. A. Celis, M. N. Nair, A. Taleb-Ibrahimi, E. H. Conrad, C. Berger, W. A. de Heer and A. Tejeda, *J. Phys. D: Appl. Phys.*, 2016, **49**, 143001.
64. O. V. Zakharova, E. E. Mastalygina, K. S. Golokhvast and A. A. Gusev, *Nanomaterials*, 2021, **11**, 2425.
65. J. H. Ho, C. L. Lu, C. C. Hwang, C. P. Chang and M. F. Lin, *Phys. Rev. B*, 2006, **74**, 085406.
66. C. L. Lu, C. P. Chang, Y. C. Huang, J. H. Ho, C. C. Hwang and M. F. Lin, *J. Phys. Soc. Jpn.*, 2007, **76**, 024701.
67. S. Okada and T. Kobayashi, *Jpn. J. Appl. Phys.*, 2009, **48**, 050207.
68. Y. P. Yang, Y. C. Zou, C. R. Woods, Y. M. Shi, J. Yin, S. G. Xu, S. Ozdemir, T. Taniguchi, K. Watanabe, A. K. Geim, K. S. Novoselov, S. J. Haigh and A. Mishchenko, *Nano Lett.*, 2019, **19**, 8526-8532.
69. P. Shi, T. Li, R. Zhang, X. Shen, X. B. Cheng, R. Xu, J. Q. Huang, X. R. Chen, H. Liu and Q. Zhang, *Adv. Mater.*, 2019, **31**.
70. J. Heyd and G. E. Scuseria, *J. Chem. Phys.*, 2004, **121**, 1187-1192.
71. M. Obata, M. Nakamura, I. Hamada and T. Oda, *J. Phys. Soc. Jpn.*, 2013, **82**, 093701.
72. P. Ruffieux, J. M. Cai, N. C. Plumb, L. Patthey, D. Prezzi, A. Ferretti, E. Molinari, X. L. Feng, K. Mullen, C. A. Pignedoli and R. Fasel, *Acs Nano*, 2012, **6**, 6930-6935.

73. B. V. Senkovskiy, A. V. Fedorov, D. Haberer, M. Farjam, K. A. Simonov, A. B. Preobrajenski, N. Martensson, N. Atodiresei, V. Caciuc, S. Blugel, A. Rosch, N. I. Verbitskiy, M. Hell, D. V. Evtushinsky, R. German, T. Marangoni, P. H. M. van Loosdrecht, F. R. Fischer and A. Gruneis, *Adv. Electron. Mater.*, 2017, **3**.
74. J. W. Chen, H. C. Huang, D. Convertino, C. Coletti, L. Y. Chang, H. W. Shiu, C. M. Cheng, M. F. Lin, S. Heun, F. S. S. Chien, Y. C. Chen, C. H. Chen and C. L. Wu, *Carbon*, 2016, **109**, 300-305.
75. C. Virojanadara, S. Watcharinyanon, A. A. Zakharov and L. I. Johansson, *Phys. Rev. B*, 2010, **82**, 205402.
76. H. Sode, L. Talirz, O. Groning, C. A. Pignedoli, R. Berger, X. L. Feng, K. Mullen, R. Fasel and P. Ruffieux, *Phys. Rev. B*, 2015, **91**.
77. Y. C. Chen, D. G. de Oteyza, Z. Pedramrazi, C. Chen, F. R. Fischer and M. F. Crommie, *Acs Nano*, 2013, **7**, 6123-6128.
78. L. Tapaszto, G. Dobrik, P. Lambin and L. P. Biro, *Nat. Nanotechnol.*, 2008, **3**, 397-401.
79. T. E. Weller, M. Ellerby, S. S. Saxena, R. P. Smith and N. T. Skipper, *Nat. Phys.*, 2005, **1**, 39-41.
80. S. Heguri, N. Kawade, T. Fujisawa, A. Yamaguchi, A. Sumiyama, K. Tanigaki and M. Kobayashi, *Phys. Rev. Lett.*, 2015, **114**., 247201.
81. M. Calandra and F. Mauri, *Phys. Rev. Lett.*, 2005, **95**, 237002.
82. Mazin, II, *Phys. Rev. Lett.*, 2005, **95**, 227001.
83. G. Profeta, M. Calandra and F. Mauri, *Nat. Phys.*, 2012, **8**, 131-134.